Observing the Quantization of Zero Mass Carriers in Graphene

David L. Miller, *et al.*

Science **324**, 924 (2009);
DOI: 10.1126/science.1171810

Observing the Quantization of Zero Mass Carriers in Graphene

David L. Miller,[1]* Kevin D. Kubista,[1]* Gregory M. Rutter,[2] Ming Ruan,[1] Walt A. de Heer,[1] Phillip N. First,[1]† Joseph A. Stroscio[2]†

Application of a magnetic field to conductors causes the charge carriers to circulate in cyclotron orbits with quantized energies called Landau levels (LLs). These are equally spaced in normal metals and two-dimensional electron gases. In graphene, however, the charge carrier velocity is independent of their energy (like massless photons). Consequently, the LL energies are not equally spaced and include a characteristic zero-energy state (the $n = 0$ LL). With the use of scanning tunneling spectroscopy of graphene grown on silicon carbide, we directly observed the discrete, non-equally–spaced energy-level spectrum of LLs, including the hallmark zero-energy state of graphene. We also detected characteristic magneto-oscillations in the tunneling conductance and mapped the electrostatic potential of graphene by measuring spatial variations in the energy of the $n = 0$ LL.

The two-dimensional (2D) form of carbon (i.e., graphene) is of interest not only because of its potential in nanoelectronics (*1*, *2*), but also because it displays several intriguing fundamental properties. One of these, the half-integer quantum Hall effect (QHE) (*3*, *4*), results from the symmetry of graphene's honeycomb crystal structure, which can be viewed as two equivalent hexagonal sublattices of carbon atoms. The same symmetry gives rise to unusual Landau levels (LLs) that are not equally spaced in energy but vary with both the square root of the magnetic field and the Landau index. This new LL spectrum, with its characteristic zero-energy state (LL index $n = 0$) is emblematic of graphene and contains information unavailable in QHE measurements. Recent LL spectra acquired on the surface of graphite are complex and have been interpreted as being dominated by graphitic stacking through several layers (*5*) or as a mixture of a Dirac-fermion spectrum and the spectrum of bulk graphite (*6*). Similar measurements for single layer graphene samples have yet to be reported, in part because of the small sample sizes obtained in the exfoliation technique. Indirect measurement of the graphene LL structure have been obtained by measuring the transitions between LLs through the use of cyclotron resonance (*7*, *8*).

In this report, we present scanning tunneling spectroscopy (STS) measurements of the graphene Landau quantization in samples grown on SiC. These experiments are free of the complications of previous studies because the graphene layers grown on SiC are electronically decoupled (*9*). We demonstrate an innovative STS measurement technique with tunneling magneto-conductance oscillations (TMCOs). These magneto-oscillations are distinctly different from traditional Shubnikov–de Haas oscillations (SdHOs) in transport measurements, as they measure the band structure properties at a variable tunneling energy rather than a single energy at the Fermi surface. Using the TMCO measurements, we map the low-energy dispersion of graphene with an energy resolution of 2.8 meV, and we extend these measurements of energy versus momentum into the empty electronic states that are inaccessible to photoelectron spectroscopy. A fundamental characteristic of quantized cyclotron orbits in graphene is the $n = 0$ LL (LL_0) made up of both electron and hole carriers and located at exactly E_D, the energy of the Dirac (charge neutrality) point. We determined the local electrostatic potential of graphene on SiC with atomic scale resolution by spatially mapping the variation in LL_0. We find the spatial variation of the local potential to be smoother than previously observed in exfoliated graphene on SiO_2 substrates (*10*, *11*).

The experiments were performed at 4.3 K in a custom-built cryogenic ultrahigh vacuum scanning tunneling microscope (STM) with high-magnetic-field capability. Multiple layers of graphene were grown on the hydrogen-etched carbon-face of 4H−SiC$(000\bar{1})$, via a low-vacuum induction furnace method (*12*), to a thickness of 10 ± 1 layers, as determined by ellipsometry (*13*). TMCO measurements, described below, were performed by sweeping the magnetic field at 0.04 T/min and measuring dI/dV with a lock-in amplifier at constant tunneling current and sample bias. dI/dV spectra as a function of tunneling bias were recorded in constant magnetic field with the tip-sample distance held fixed and using a root

[1]School of Physics, Georgia Institute of Technology, Atlanta, GA 30332, USA. [2]Center for Nanoscale Science and Technology, National Institute of Standards and Technology (NIST), Gaithersburg, MD 20899, USA.

*These authors contributed equally to this work.
†To whom correspondence should be addressed: first@physics.gatech.edu (P.N.F.); joseph.stroscio@nist.gov (J.A.S.)

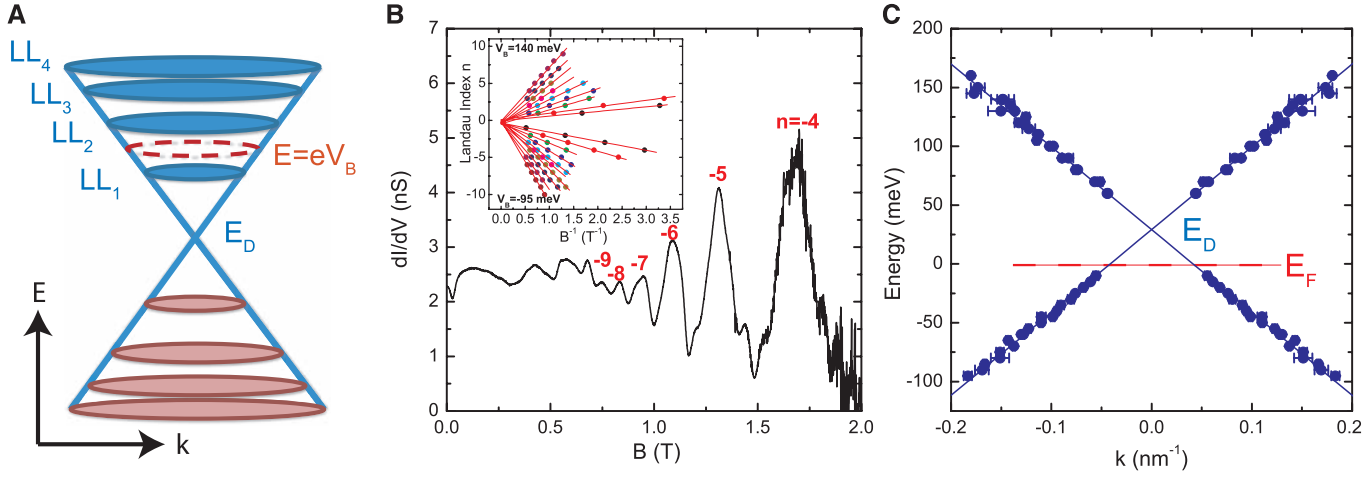

Fig. 1. TMCOs in epitaxial graphene. (**A**) Schematic of graphene low-energy dispersion with quantized LLs (LL_n) in a magnetic field. The Dirac point E_D locates the common apex of the electron and hole cones. The red dashed line indicates the k-space area A_E corresponding to a dI/dV measurement at the set-point energy $E = eV_B$. (**B**) TMCOs in dI/dV ($E = -65$ meV) as the magnetic field is swept perpendicular to the graphene plane. The largest oscillations originate from the LLs sweeping through the energy E. (Inset) Fan plot showing a linear relation in the LL index n from the conductance oscillations versus $1/B$, yielding the TMCO frequencies B_E. The error in the peak positions is smaller than the symbol size, and each line corresponds to a separate TMCO measurement at different tunneling biases from −95 to 140 mV [see fig. S1 (*13*)]. (**C**) The energy-momentum dispersion (symmetrized about $k = 0$) obtained from the TMCO frequencies B_E. A linear fit yields a carrier velocity $c^* = (1.070 \pm 0.006) \times 10^6$ ms^{-1} and a Dirac point location of $E_D = 29.7 \pm 0.5$ meV above E_F (*20*).

mean square modulation voltage of 1 mV superimposed on the sample bias at a frequency of 500 Hz. These two methods are complementary, as they each measure a dI/dV slice in the 2D magnetic field, energy (B, E) plane at either fixed E (TMCO spectra) or fixed B [conventional $dI/dV(E)$ spectra].

A schematic of the low-energy electronic structure for graphene (Fig. 1A) shows the two symmetric Dirac cones that meet at the Dirac point (E_D), where the density of carriers vanishes. Applying a perpendicular magnetic field causes the electron and hole states to condense into LLs, indicated by the projected circular cross sections intersecting the conical dispersion. Unlike conventional 2D systems with a parabolic dispersion, the LL energies E_n of graphene are not equally spaced: $E_n = \mathrm{sgn}(n)c^*\sqrt{2e\hbar B|n|}$, $n = -2, -1, 0, 1, 2,\ldots$ (Fig. 1A), where c^* is the characteristic carrier velocity, e is the elementary charge, and $\hbar$ is Planck's constant h divided by 2π. In addition, the unique $n = 0$ LL at $E_0 = E_D$ is not present in a conventional 2D system and is at the heart of the half-integer QHE in graphene. The physics of the $n = 0$ LL itself is presently under active theoretical study due to expectations of unique topological and correlation phenomena and because of its effect on screening (*14*, *15*).

Physical measurements of Landau-quantized systems exhibit characteristic oscillations in many properties as the LLs move through the Fermi level (E_F) with changing magnetic field. The most well-known magneto-oscillations in 2D electron systems are SdHOs in the magnetoresistance, which can be used to determine Fermi-surface properties. In Fig. 1B, we show TMCOs; a set of increasing oscillations were observed in the STS dI/dV signal from epitaxial graphene as the magnetic field was swept from 0 to 2.0 T at a tunneling bias of −65mV. These oscillations are analogous to SdHOs in conventional magnetoresistance measurements; however, TMCOs are not restricted to E_F. The oscillations vary as a function of energy E, with $E - E_F = eV_B$ determined by the tunneling bias and where E_F corresponds to $V_B = 0$ (Fig. 1A). (In what follows, we take E_F as the zero of energy for convenience.) As indicated in Fig. 1A, the dI/dV signal will oscillate with the density of states because the LLs move through the energy position $E = eV_B$; a maximum in dI/dV occurs at fields where $E_n = eV_B$ (Fig. 1B). For SdHOs, the frequency of oscillations in $1/B$ is given by $B_F = (\hbar/2\pi e)A_F$, where A_F is the cross-sectional area of the Fermi surface in a plane normal to the magnetic field (*16*–*18*). In our measurements, the TMCO frequency B_E is given by a similar expression, except that A_F is replaced by A_E, where A_E is the cross-sectional k-space area at energy $E = eV_B$ (Fig. 1A). This difference is crucial as it allows the TMCO measurements to determine the low-energy electronic band structure with very high resolution in both energy and crystal momentum as E is varied via the tunneling bias. This simple distinction makes the TMCO technique potentially applicable to a wide range of materials because no gate electrode is required.

For graphene, we assume circular constant-energy contours of area $A_E = \pi k_E^2$ to determine the graphene wave vector $k_E = [(4\pi e/h)B_E]^{1/2}$. The inset to Fig. 1B shows a "fan plot" of LL index measured from the TMCO peak maxima versus $1/B$ for different values of tunneling bias V_B. This analysis yielded a range of oscillation frequencies B_E corresponding to different constant energy contours A_E [see fig. S1 (*13*)]. The zero inverse-field intercept of each line in the fan plot is sensitive to the chirality of the graphene wave function, which can be described by a pseudo-spinor. The fan plot intercepts all fall near zero, indicating a Berry phase of π (*19*); thus, the multilayer epitaxial graphene system exhibits the pseudo-spin of massless Dirac fermions. Figure 1C shows the linear energy-momentum dispersion determined from the TMCO measurements for energies within ±125 meV of E_D. A linear fit to the TMCO dispersion data (solid lines in Fig. 1C) determines a velocity for this epitaxial graphene system of $c^* = (1.070 \pm 0.006) \times 10^6$ ms^{-1} for both electrons and holes (*20*), with the Dirac point energy 29.7 ± 0.5 meV above the Fermi level (the range of observed E_D values is discussed below). The TMCO measurement in Fig. 1C represents a high-accuracy determination of the graphene dispersion, with an energy resolution (2.8 meV) limited by the thermal and instrumental broadening at 4.3 K and a wave-vector resolution of ≤0.02 nm^{-1}. This high-resolution measurement also includes the unfilled electronic states, a regime that is not accessible by photoelectron measurements (*21*, *22*).

The Landau quantization of the density of states was directly measured in the dI/dV spectra at fixed magnetic field. Figure 2A shows a direct measurement of the graphene quantization with over 20 LLs observed in the tunneling spectrum in an applied field of 5 T. The LL peaks are extremely sharp as compared with similar spectra from semiconductor 2D electron systems or bulk graphite (*5*, *6*, *23*). Evidence for massless Dirac fermions can be easily inferred by the observation of the LL_0 peak at 7 mV and the large energy gaps on either side of LL_0 with zero differential conductance. Small features in the spectrum near

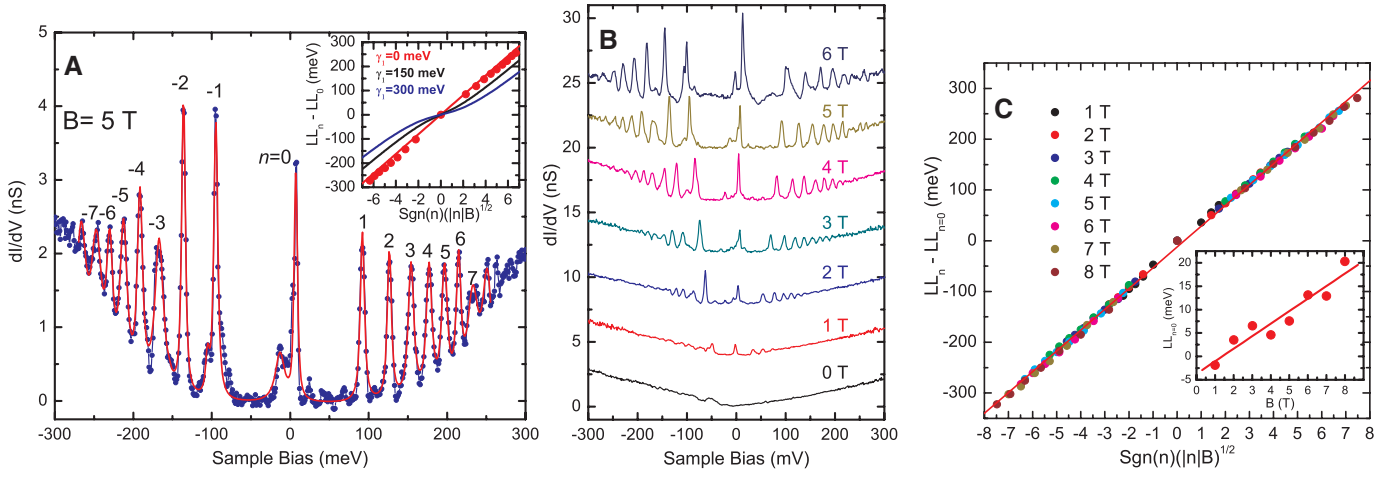

Fig. 2. Direct measurement of Landau quantization in epitaxial graphene. (**A**) Blue data points show the tunneling differential conductance spectra versus sample bias of LLs in multilayer graphene at $B = 5$ T. LL indices are marked. The red line shows a fit to a series of Voigt line shapes at the LL peak positions, which accounts for essentially all the density of states in the spectrum (tunneling set point, $V_B = 350$ mV, $I = 400$ pA). (Inset) LL peak position versus square root of LL index and applied field from the peak positions in (A). Errors in peak positions are smaller than the symbol size. Solid lines are fits to a bilayer model with interlayer coupling of zero (red), 150 meV (black), and 300 meV (blue). (**B**) LL spectra for various applied magnetic fields from 0 to 6 T. The curves are offset for clarity (tunneling set point, $V_B = 350$ mV, $I = 400$ pA). (**C**) LL peak energies for applied fields of 1 to 8 T, showing a collapse of the data when plotted versus square root of LL index and applied field. The solid line shows a linear fit yielding a characteristic velocity of $c^* = (1.128 \pm 0.004) \times 10^6$ ms^{-1} (*20*). (Inset) The shift in the LL_0 peak position as a function of applied field (symbols). The error is smaller than the symbol size. The solid line is a linear fit to the data points.

the $n = 0$ and $n = -1$ LLs remain unexplained; these may arise from defect scattering, as they vary somewhat with spatial position (Fig. 3), or they may be intrinsic fine structure of the LL states, particularly for the $n = 0$ LL, where electron correlations may lift the fourfold degeneracy (*24*). The LL spectrum in Fig. 2A fits well to a simple sum of Voigt line shapes; i.e., Lorentzians with variable energy widths convolved with a single Gaussian instrument function of 2.8-meV full width at half maximum. The Gaussian models both thermal and instrumental (bias modulation) contributions. As shown by the red line in Fig. 2A, the fit accounts for essentially all of the original spectral weight in the density of states. The rising background is dominated by the Lorentzian tails of each LL, which are determined by the carrier lifetimes, and all the density of states is quantized into the LLs. The observed linewidths of the LLs were very small. In particular, we measured a Lorenztian linewidth of 1.5 meV for LL_0 at $B = 5$ T (Fig. 2A). Associating this width with a characteristic scattering time $\tau = \hbar/\Delta E$ yields $\tau = 0.4$ ps. This scattering time is comparable to or larger than that observed in the highest mobility suspended graphene samples (*25*) and multilayer epitaxial graphene samples (*26*), with reported mobilities exceeding 200,000 $cm^2\ V^{-1}\ s^{-1}$.

Previous tunneling spectroscopy measurements on graphite samples have shown quantization that varied linearly in magnetic field (*5*) instead of the square-root dependence expected for graphene or contained a complex mixture of spectral peaks that exhibited both equally and non-equally–spaced LLs (*6*). The ability to observe pure graphene quantization in these results stems from the decoupled nature of the graphene layers grown on SiC (*9*). To investigate quantitatively the coupling between graphene layers in this multilayer sample, we fit the LL energies in Fig. 2A to a bilayer model for different values of the interlayer coupling γ_1 (Fig. 2A, inset) (*27*). An interlayer coupling of 300 to 400 meV has been measured for Bernal-stacked graphene bilayers (*28*, *29*), yet the best fit to the spectrum in Fig. 2A clearly indicates zero-interlayer coupling ($\gamma_1 = 0$). We discuss the origin of these decoupled graphene layers on SiC below.

Figure 2B shows a series of *dI*/*dV* spectra for different magnetic fields. The LL peaks increased in intensity with increasing energy separation as the magnetic field is increased. A slight shift of LL_0 was also observed with increasing field. The Dirac point E_D lies below the Fermi level at low fields (–1.8 meV at 1 T) and shifts to a position of 13.1 meV above E_F at 6 T (Fig. 2C, inset). Extrapolating the LL_0 position to zero field yields a Dirac point $E_D = -3.7$ meV at $B = 0$, corresponding to an electron doping of $n = 8.8 \times 10^8\ cm^{-2}$. This low charge density in the top layer results from the decay in the charge profile through the multilayer stack from the highly doped interface layer and is similar to that seen in optical measurements (*7*). The shift of the Dirac point with field results from the redistribution of charge in the multilayer determined by the degeneracy of the available LLs and the effective screening perpendicular to the graphene planes. The shift of LL_0 across the Fermi level is not completely understood at present and could be influenced by the electrostatic potential derived from the difference in the probe tip and graphene work functions. A more detailed theoretical analysis of the screening properties of Dirac carriers in the presence of a tip potential and a constant magnetic field would be required for a complete understanding of these results.

The spectrum of LLs in Fig. 2A demonstrates the direct measurement of the massless Dirac-fermion quantization in graphene. Further confirmation of graphene quantization and electronic structure comes from the scaling of LL energies E_n with magnetic field at high fields. For massless Dirac fermions in graphene, the spectrum E_n should scale as $\sqrt{B}$, whereas in all other forms (including bilayer graphene and graphite), the LLs scale linearly in B for energies near the Dirac point. Notably, a complete linear collapse of all of the LLs energies is obtained by plotting E_n versus $\sqrt{|n|B}$ (Fig. 2C), which is a distinct signature of graphene quantization. Fitting both electron and hole branches in Fig. 2C yields a common carrier velocity of $c^* = (1.128 \pm 0.004) \times 10^6\ ms^{-1}$, confirming massless Dirac fermions in this epitaxial graphene system and in good agreement with the range of values reported for graphene from other techniques (*8*).

Close inspection of Fig. 2C shows that the electron and hole states actually have slightly different velocities. Independent fits to the two branches give velocities $c^* = (1.189 \pm 0.007) \times 10^6\ ms^{-1}$ for the states below E_D and $c^* = (1.044 \pm 0.004) \times 10^6\ ms^{-1}$ for states above E_D. The 6%

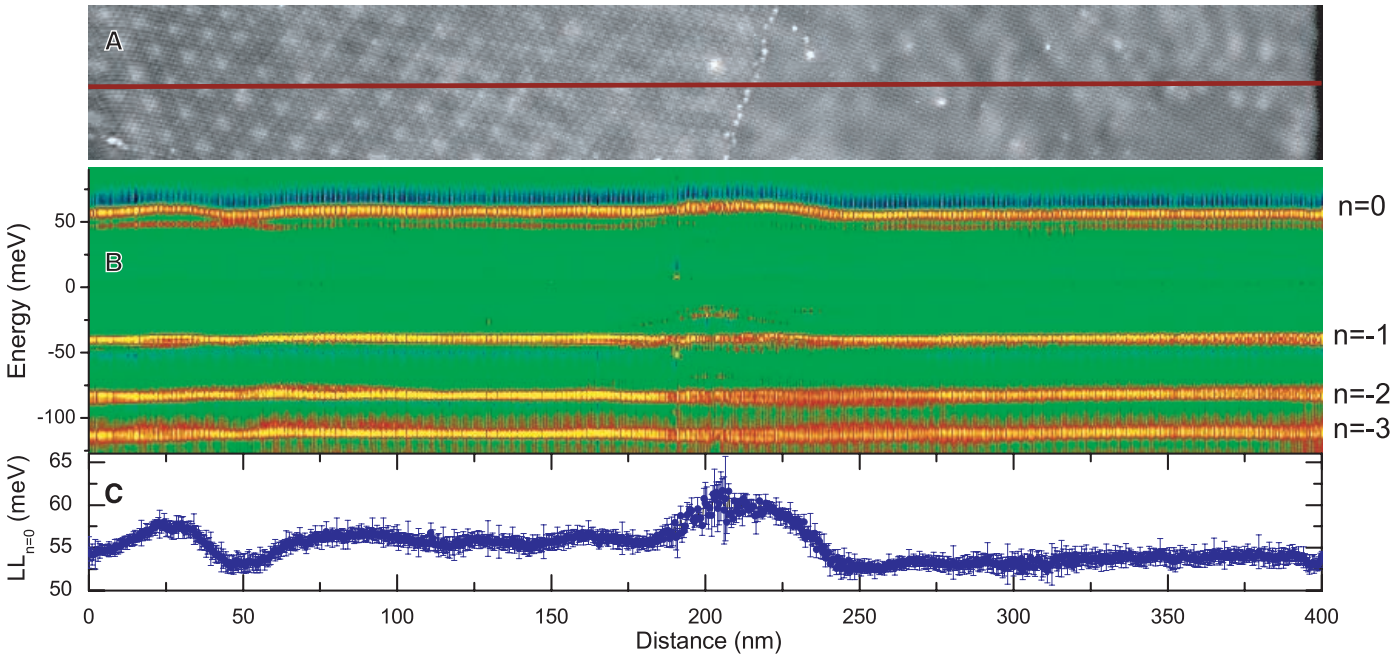

Fig. 3. Spatial variation of the surface potential in epitaxial graphene. (**A**) STM topograph (50 by 400 nm) showing a region containing a boundary between two different moiré regions. The gray scale range is 0.3 nm, and the periodic features correspond to the moiré [see fig. S2 (*13*)]. (**B**) A series of *dI*/*dV* spectra obtained along the center horizontal line in (A) showing low-lying LLs. $B = 5$ T. Image color is the *dI*/*dV* intensity (blue: –1.5 nS to yellow: 2.5 nS), the horizontal axis is distance, and the vertical axis is energy. The LL indices are labeled to the right of the image. (**C**) Variation in the LL_0 peak position as a function of distance along the line indicated in (A). Error bars are 1σ error in fitting LL_0 peak positions in (B).

difference observed between these values may imply a breakdown of electron-hole symmetry because of many-body effects (*8*, *30*). However, some contribution to the electron-hole asymmetry observed in Fig. 2C could also be caused by the screening of the tip electric field (band bending), requiring a small correction to the energy scale in Fig. 2C.

Spatial variation of the LL energies can be used to map fluctuations of the local potential (*31*), as we show for the $n = 0$ LL (Fig. 3). This level, composed of electron and hole carriers, occurs exactly at the Dirac point, as a direct consequence of the chiral solutions of the Dirac equation that describes graphene's low-energy electronic structure. Figure 3, A and B, shows a topographic image and corresponding spatial map of the lowest LL_n energies (vertical) and dI/dV intensities (color scale) for $n = 0, -1, -2$, and -3 along the line marked in Fig. 3A. The average position of E_D was 55.2 meV above E_F, with a SD of ±1.9 meV (Fig. 3C) (*20*). By far, the largest variation (in this image and generally in our measurements) corresponded to a subsurface rotational domain boundary that occurs in the center of the image [the top graphene layer is atomically continuous over the boundary (fig. S3)]. Away from such boundaries, the spatial fluctuations were much smaller: ≈0.5 meV, as seen for the region from 250 to 400 nm in Fig. 3. The Dirac point energy map showed an extremely smooth potential (hence, small carrier density fluctuations) for this low-doped graphene sheet, in contrast to the electron and hole puddles observed for exfoliated graphene on SiO_2 substrates (*10*). In surveying the sample, a variation of ~±25 meV in E_D was observed over distances of many tens of micrometers (see E_D differences between Figs. 2 and 3). The larger density fluctuations on SiO_2 substrates apparently result from charged impurities in the SiO_2 substrate. The smooth charge/potential contour in epitaxial graphene could be the result of screening of the interface potential fluctuations by the graphene multilayer, and the crystalline SiC substrate may be more homogenous than the amorphous SiO_2 substrate with respect to trapped charges.

The dI/dV spectra in Fig. 2 show a direct measurement of graphene magnetic quantization expected for massless Dirac fermions. This result implies that the topmost layer of epitaxial graphene closely approximates an isolated sheet of graphene. We attribute this isolation to the presence of rotational stacking faults between the graphene layers in epitaxial graphene grown on the carbon face of SiC, which effectively decouples the electronic structure of the layers (*9*). A variety of rotational stacking angles were found in STM topographic images of the surface (fig. S2) (*13*). Slight rotations of one layer with respect to the next create moiré super periods superimposed on the atomic lattice (fig. S2) (*9*, *13*). The ≈0.02-nm peak-to-peak height modulation originates from periodically varying the alignment of top-layer atoms with those below, but the exact source of image contrast is still a subject of debate (*32*). Our survey of the carbon-face grown sample showed moiré patterns of various periods in almost every location examined, with spectra similar to those seen in Fig. 2. We expect this structure of multilayer epitaxial graphene to be important for future studies of Dirac point physics in graphene.

Note added in proof: A new publication reports the observation of graphene LLs in STS measurements over a graphene flake on graphite (*33*).

References and Notes

1. C. Berger *et al.*, *J. Phys. Chem. B* **108**, 19912 (2004).
2. C. Berger *et al.*, *Science* **312**, 1191 (2006); published online 12 April 2006 (10.1126/science.1125925).
3. K. S. Novoselov *et al.*, *Nature* **438**, 197 (2005).
4. Y. Zhang, Y. W. Tan, H. L. Stormer, P. Kim, *Nature* **438**, 201 (2005).
5. T. Matsui *et al.*, *Phys. Rev. Lett.* **94**, 226403 (2005).
6. G. Li, E. Y. Andrei, *Nat. Phys.* **3**, 623 (2007).
7. M. L. Sadowski, G. Martinez, M. Potemski, C. Berger, W. A. de Heer, *Phys. Rev. Lett.* **97**, 266405 (2006).
8. R. S. Deacon, K. C. Chuang, R. J. Nicholas, K. S. Novoselov, A. K. Geim, *Phys. Rev. B* **76**, 081406R (2007).
9. J. Hass *et al.*, *Phys. Rev. Lett.* **100**, 125504 (2008).
10. J. Martin *et al.*, *Nat. Phys.* **4**, 144 (2008).
11. E. Rossi, S. Das Sarma, *Phys. Rev. Lett.* **101**, 166803 (2008).
12. W. A. de Heer *et al.*, *Solid State Commun.* **143**, 92 (2007).
13. Additional text and data are available on *Science* Online.
14. C. Toke, P. E. Lammert, V. H. Crespi, J. K. Jain, *Phys. Rev. B* **74**, 235417 (2006).
15. M. Arikawa, Y. Hatsugai, H. Aoki, *Phys. Rev. B* **78**, 205401 (2008).
16. N. Ashcroft, N. Mermin, *Solid State Physics* (Brooks Cole, London, 1976).
17. V. P. Gusynin, S. G. Sharapov, *Phys. Rev. B* **71**, 125124 (2005).
18. S. G. Sharapov, V. P. Gusynin, H. Beck, *Phys. Rev. B* **69**, 075104 (2004).
19. I. A. Luk'yanchuk, Y. Kopelevich, *Phys. Rev. Lett.* **93**, 166402 (2004).
20. All uncertainties reported represent 1 SD in the measured quantity.
21. E. Rollings *et al.*, *J. Phys. Chem. Solids* **67**, 2172 (2006).
22. A. Bostwick, T. Ohta, T. Seyller, K. Horn, E. Rotenberg, *Nat. Phys.* **3**, 36 (2007).
23. M. Morgenstern, J. Klijn, C. Meyer, R. Wiesendanger, *Phys. Rev. Lett.* **90**, 056804 (2003).
24. Y. Zhang *et al.*, *Phys. Rev. Lett.* **96**, 136806 (2006).
25. K. I. Bolotin *et al.*, *Solid State Commun.* **146**, 351 (2008).
26. M. Orlita *et al.*, *Phys. Rev. Lett.* **101**, 267601 (2008).
27. E. A. Henriksen *et al.*, *Phys. Rev. Lett.* **100**, 087403 (2008).
28. G. M. Rutter, J. N. Crain, N. P. Guisinger, P. N. First, J. A. Stroscio, *J. Vac. Sci. Technol. A* **26**, 938 (2008).
29. J. Yan, E. A. Henriksen, P. Kim, A. Pinczuk, *Phys. Rev. Lett.* **101**, 136804 (2008).
30. P. E. Trevisanutto, C. Giorgetti, L. Reining, M. Ladisa, V. Olevano, *Phys. Rev. Lett.* **101**, 226405 (2008).
31. M. Morgenstern, C. Wittneven, R. Dombrowski, R. Wiesendanger, *Phys. Rev. Lett.* **84**, 5588 (2000).
32. W. T. Pong, C. Durkan, *J. Phys. D Appl. Phys.* **38**, R329 (2005).
33. G. Li, A. Luican, E. Y. Andrei, *Phys. Rev. Lett.* **102**, 176804 (2009).

34. We thank A. MacDonald, H. Min, M. Stiles, and the NIST graphene team for valuable comments and discussions and C. Berger, N. Sharma, M. Sprinkle, S. Blankenship, A. Band, and F. Hess for their technical contributions to this work. Portions of this work were supported by NSF (grant ECCS-0804908), the Semiconductor Research Corporation Nanoelectronics Research Initiative (INDEX program), and the W. M. Keck Foundation. Graphene production facilities were developed under NSF grant ECCS-0521041.

Supporting Online Material

www.sciencemag.org/cgi/content/full/324/5929/924/DC1
SOM Text
Figs. S1 to S3

3 February 2009; accepted 17 March 2009
10.1126/science.1171810

Direct Detection of Abortive RNA Transcripts in Vivo

Seth R. Goldman,[1] Richard H. Ebright,[2] Bryce E. Nickels[1]*

During transcription initiation in vitro, prokaryotic and eukaryotic RNA polymerase (RNAP) can engage in abortive initiation—the synthesis and release of short (2 to 15 nucleotides) RNA transcripts—before productive initiation. It has not been known whether abortive initiation occurs in vivo. Using hybridization with locked nucleic acid probes, we directly detected abortive transcripts in bacteria. In addition, we show that in vivo abortive initiation shows characteristics of in vitro abortive initiation: Abortive initiation increases upon stabilizing interactions between RNAP and either promoter DNA or sigma factor, and also upon deleting elongation factor GreA. Abortive transcripts may have functional roles in regulating gene expression in vivo.

During transcription, RNA polymerase (RNAP) synthesizes the first ~8 to 15 nucleotides (nt) of RNA as an RNAP-promoter initial transcribing complex (*1*–*3*) [using a "scrunching" mechanism (*4*)]. Upon synthesis of an RNA transcript with a threshold length of ~8 to 15 nt, RNAP breaks its interactions with promoter DNA, escapes the promoter, and enters into processive synthesis of RNA as an RNAP-DNA transcription elongation complex (*1*–*3*) [using a "stepping" mechanism (*5*)]. In transcription reactions in vitro, the RNAP-promoter initial transcribing complex can engage in tens to hundreds of cycles of synthesis and release of short RNA transcripts (abortive initiation) (*1*–*3*, *6*–*8*). Abortive initiation competes with productive initiation in vitro and, as such, is a critical determinant of promoter strength and a target of transcription regulation in vitro (*1*–*3*, *7*–*13*). It has been proposed that abortive initiation likewise occurs in vivo

[1]Department of Genetics and Waksman Institute, Rutgers University, Piscataway, NJ 08854, USA. [2]Department of Chemistry, Waksman Institute, and Howard Hughes Medical Institute, Rutgers University, Piscataway, NJ 08854, USA.

*To whom correspondence should be addressed. E-mail: bnickels@waksman.rutgers.edu